Active and Passive Lenses From Coupled Square Ring Slots

CHRISTOPH KOHLBERGER [1] **(Graduate Student Member, IEEE), SAEID KARAMZADEH** [2,3] **(Member, IEEE), AND ANDREAS STELZER** [1] **(Member, IEEE)**

(Regular Paper)

[1]Institute for Communications Engineering and RF-Systems, Johannes Kepler University Linz, 4040 Linz, Austria
[2]Millimeter Wave Technologies, Intelligent Wireless System, Silicon Austria Labs (SAL), 4040 Linz, Austria
[3]Electrical and Electronics Engineering Department, Bahçeşehir University, Istanbul 34349, Türkiye

CORRESPONDING AUTHOR: Christoph Kohlberger (e-mail: christophkohlberger@gmail.com).

ABSTRACT This work presents the utilization of square ring slots as resonators on active and passive metasurfaces operating within the K_a-band. Thereby, fully functional prototypes of reflectors and lenses based on a two-layer printed circuit board were fabricated and verified. The analytical model of the square ring slot structure is depicted extensively, which allows finding simulation optimized designs that can be applied to the passive prototypes. Additionally, the gained information on self-resonances is used for combinations with layers, activated through lumped varactor diodes. In the end, the reflection and transmission parameters of single active and passive designs as well as beam patterns of the lenses are measured and interpreted, resulting in a switching dynamic range of 15 dB at a bandwidth of 1 GHz for active reflectors and a maximum gain of 22 dBi at 26 GHz for the passive lens. While the active lens operates best approximately 1 GHz around the design frequency at 26 GHz, the passive one maintains a maximum gain higher than 20.8 dBi between 23 and 27 GHz.

INDEX TERMS Active metamaterial, equivalent circuit, frequency selective surface, Fresnel lens, lens antenna, reflect array, square ring slot, surface resonator.

I. INTRODUCTION

Metasurfaces remain a promising candidate to revolutionize microwave and antenna technology as thin and lightweight wave manipulating structures [1], [2], [3], [4]. Besides the application of passive designs in e.g. perfect reflectors, wide bandwidth absorbers or thin lenses, active metamaterial gains interest from recent investigation in communication technology and antenna systems [5], [6]. The potential of guiding reflected and transmitted radiation by phase shifting surfaces motivates academic as well as industrial research.

Thin lenses from passive metasurfaces operating up to very high frequencies were designed, fabricated, and tested successfully in the past decade. On the one hand, this was made possible by utilizing multilayer structures that behave similar to high order bandpasses and therefore exhibit sufficient phase

shift while providing high transmission [7], [8], [9], [10], [11]. Thereby, the individual layers consist of simple grids or patch arrays that behave either inductive or capacitive [12]. On the other hand, additive manufacturing can be used to modify the density of dielectric material and hence its permittivity. The effects of such 3-D printed lenses can be enhanced using additional metal structures [13], [14], [15]. Besides this, reflectors with partly more complicated layer designs that are connected to active components are capable of absorption tuning [16], [17] and beam steering [18], [19]. At reflecting surfaces, lower order scatterers already provide enough phase shift to properly manipulate waves, enabling fully functional systems on two-layer structures. In this work, periodically arranged square ring slots (SRS) are used to build active and passive transmit arrays on simple double layer printed
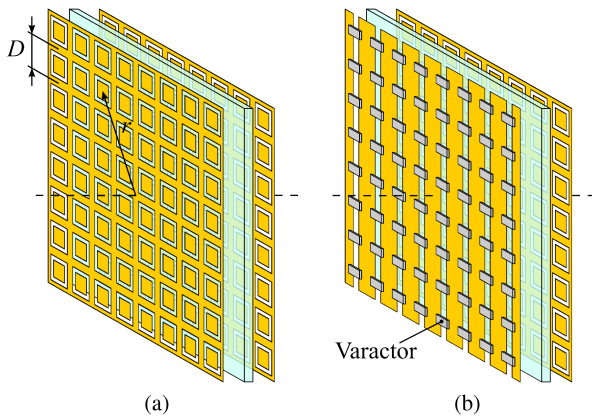
FIGURE 1. Basic build-up of passive (a) and active (b) 2-layer PCB with SRS structures RO4350 dielectric. The images show the periodicity *D* and radial element position *r* from the array center.

FIGURE 2. (a) Simplified electrodynamic behaviour of an SRS under an alternating vertically polarized electric field *E*. The black arrows correspond to current densities resulting in self-inductance. Accumulated charges at the structure edges lead to capacitive effects between the grid and the patch and within the grid itself (grey arrows). (b) Structure dimensions that define the SRS and are related to the dominant EQC parameters L_g and C_p.

circuit boards (PCB) as shown in Fig. 1. The SRS exhibits thereby a first order resonance on a solitary metal sheet, as the corresponding equivalent circuit (EQC) consists of a shunt capacitance and a shunt inductance. Analytical expressions for the corresponding EQC components can be derived from investigations on the square loop [20], [21], [22], which was presented in [23]. There, both structures are examined analytically, with simulations, and through measurements. Resulting expressions are similar to those of simple grids and patch arrays from [12], [24], [25], enabling to solve the inverse metamaterial design problem. The same concept can be applied to more sophisticated meander loops and slots [26], [27] to induce additional capacitance and inductance.

Consequently, the combined shunt capacitance and inductance of single SRS layers can be incorporated into EQCs of multi-layer systems that represent higher order bandpasses [28], [29], [30]. The simplified model of EQC components and evanescent interactions between the layers, however, corrupt the behaviour of analytically designed bandpass structures [31], [32]. Therefore, multi-layer systems often require optimization through iterative full-wave simulations [10].

Since active or passive lumped elements exhibit intrinsic resonances themselves, their application to simple metasurfaces result in promising behaviour especially at high frequencies [33]. As for surfaces without discrete circuit elements, the combination with resonating structures as e.g. SRS can increase the resonance order of the whole system, enabling sharper notches or operation across a broader frequency band [31], [34], [35].

The work here, presents the utilization of established SRS structures firstly on passive transmit arrays as thin lenses and secondly in combination with active elements as tunable reflectors. Thereby, lenses that solely require two metal layers are characterized in lens-antenna systems through beam-pattern measurements and compared to similar existing solutions. Active metasurfaces, consisting of SRS structures on the one side and varactor biased slits on the other side, are
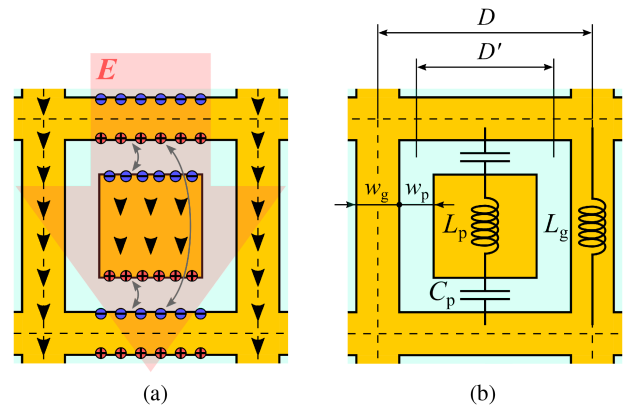
designed by investigating self resonances and verified through over-the-air (OTA) S-parameter measurements. Finally, the active SRS designs are utilized on an active double layer lens.

II. SQUARE RING SLOT MODEL

As stated above, a single layer SRS corresponds to a parallel LC shunt, where the EQC parameters are strongly related to those of simple grids and patch arrays [23]. To illustrate this, Fig. 2 depicts the induction of surface currents and charge separation at a metasurface under an alternating electric field. These effects can be related to inductive and capacitive behaviour, where the magnitudes of corresponding circuit parameters are mainly related to the structure dimensions. The inductance of the outer grid L_g depends on the structure periodicity D and the grid width w_g, which coincides with the EQC solution for plain grids

$$L_g = \frac{\mu_0 D}{2\pi} \log\left(\frac{1}{\sin\left(\frac{w_g \pi}{2D}\right)}\right). \quad (1)$$

The capacitance from the gap between the grid and the inner patch defined by w_p, however, corresponds to the equivalent capacitance of a patch array with two modifications. Firstly, the unit cell of a patch array compares rather to the inner part of the grid than to the whole SRS unit cell. Therefore, the expression $D' = D - w_g - w_p$ replaces the array periodicity D in the capacitance formula. Secondly, there are two subsequent gaps within a SRS unit cell, resulting in a series connection and subsequently a reduction of C_p by half. Both changes result in

$$C_p = \frac{\varepsilon_0 \varepsilon_{eff} D'}{\pi} \log\left(\frac{1}{\sin\left(\frac{w_p \pi}{2D'}\right)}\right) \quad (2)$$

with $\varepsilon_{eff} = (\varepsilon_r^I + \varepsilon_r^{II})/2$, where ε_r^I and ε_r^{II} are the material permittivities at both sides of the surface.

Even if the EQC parameters above do not consider the inductance of the patch L_p or the capacitance between the grid
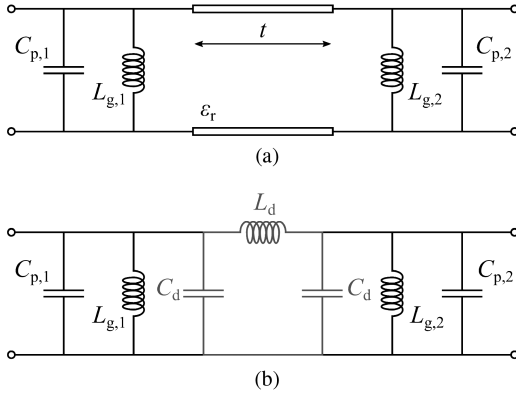
FIGURE 3. (a) Simple EQC of SRS structures on a two-layer PCB with thickness t and permittivity ε_r. (b) Modified EQC, where the tranmission line in (a) is replaced by shunt capacitors and a series inductance, as in [29]. This circuit can be directly related to a 2nd order bandpass.

rods, the resulting resonances are close to more sophisticated solutions presented in e.g. [23]. This is important as complicated formulas often cannot be solved in closed form for w_g or w_p, which indeed is essential for generating metasurface bandpass designs. The solution for w_g is straight forward and results in

$$w_g(L_g) = \frac{2D}{\pi} \arcsin\left[\exp\left(-\frac{L_g}{\mu_0}\frac{2\pi}{D}\right)\right]. \quad (3)$$

To solve expression (2) for w_p, a further simplification needs to be conducted as w_p is also in D'. Assuming that the gap width is small compared to $D - w_g$, which is valid for all the generated bandpass designs, w_p is well approximated by

$$w_p(C_p) \approx \frac{2(D - w_g)}{\pi} \arcsin\left[\exp\left(-\frac{C_p}{\varepsilon_0\varepsilon_{\text{eff}}}\frac{\pi}{D - w_g}\right)\right]. \quad (4)$$

Now that the EQC parameters of the SRS can be converted into a structural design through (1)–(4) from [12], [23], it is possible to deterministically utilize multilayer combinations as bandpasses. Thereby, every layer corresponds to a single resonator with the number of layers being equivalent to the filter order.

III. OPTIMIZATION IN COUPLED RESONATORS
In the following, 2nd order bandpass designs with different center frequencies around 26 GHz are generated and optimized. This results in easy to fabricate two-layer systems that can be built from standard printed circuit board material. A corresponding EQC of these designs is depicted in Fig. 3(a), with the center transmission line representing the dielectric. For thin slabs, this transmission line can be replaced by shunt capacitors C_d with a series inductor L_d in between, resulting in the circuit in Fig. 3(b). One sees that the SRS inductance $L_{g,i}$ resonates with the total capacitance $C_i' = C_{p,i} + C_d$ formed by the SRS structure and the dielectric. The remaining series inductance L_d couples between the two resonators.

The required bandpass circuit elements can be generated similarly as in [29] and [30] from normalized quality factors and coupling coefficients. For a 2nd order Butterworth filter, the quality factors read $q_1 = q_2 = \sqrt{2}$ and the coupling

factor is $k = \sqrt{1/2}$ with generator and load impedance being matched $r_1 = r_2 = 1$. The total capacitance per layer is then calculated by

$$C_i' = \frac{q_i}{\omega_c\eta_0 r_i\delta_{\text{BW}}}, \quad (5)$$

where $\omega_c = 2\pi f_c$ is the angular center frequency and $\delta_{\text{BW}} = \text{BW}/f_c$ is the relative filter bandwidth. Furthermore, the quality factors q_i were renormalized by the vacuum wave impedance $\eta_0 = \sqrt{\mu_0/\varepsilon_0}$. With the capacitances above, the expression for the resonator inductance, which is equal to the inductance needed at the SRS, reads

$$L_{g,i} = \frac{1}{\omega_c^2(C_i' - k\delta_{\text{BW}}\sqrt{C_1'C_2'})}. \quad (6)$$

The coupling inductance

$$L_d = \frac{1}{\omega_c^2 k\delta_{\text{BW}}\sqrt{C_1'C_2'}} \quad (7)$$

is directly proportional to the PCB thickness t according to

$$t = \frac{L_d}{\mu_0\mu_r}. \quad (8)$$

With the PCB thickness being defined, the capacitance of the SRS C_i can be calculated through

$$C_{p,i} = C_i' - \frac{\varepsilon_0\varepsilon_r t}{2}. \quad (9)$$

Expressions (8) and (9) approximate short transmission lines through a shunt capacitance and series inductances and are found in e.g. [29]. Now that all the equivalent circuit parameters of the bandpass are evaluated, it can be related to an actual metasurface by utilizing formulas (3) and (4). However, as described in [10], [11], mutual coupling that is not considered in the EQC as well as a variation of the required PCB thicknesses over different designs corrupt the frequency responses of the bandpasses. As in the former works, this issue was overcome by automated gradient optimization on the metasurface bandpass designs.

The optimization procedure was performed on 12 Butterworth filters with center frequencies f_c varying from 18 GHz to 30 GHz and a bandwidth of 11 GHz. Thereby, initial EQC calculations resulted in high coupling inductances L_d, leading to very thick dielectrics for most of the bandpass designs. Since the maximum thickness of the chosen RO4350 material ($\varepsilon_r = 3.4$ [36]) was limited to $t = 1.5$ mm, that value had to be applied to C_d in (9) for all structures. Certainly, this did not affect the frequency responses of the ideal bandpasses, as the total capacitance C_i' remained untouched. However, it influenced the extracted SRS capacitance $C_{p,i}$ to better represent the simulated and subsequently manufactured metasurfaces. The metal structures of the PCB consisted of 15 μm thick copper covered by a nickel/gold coating, which was approximated by a two-dimensional perfect conductor in the simulations.

During the optimization, a simulation-based steepest descent method, adjusted the design parameters corresponding to w_g and w_p of the two layers systematically, until the metamaterial bandpass designs matched the analytical frequency response closest. Obviously, the analytical parameters of the first surface $w_{g,1}$ and $w_{p,1}$ are equal to those of the second
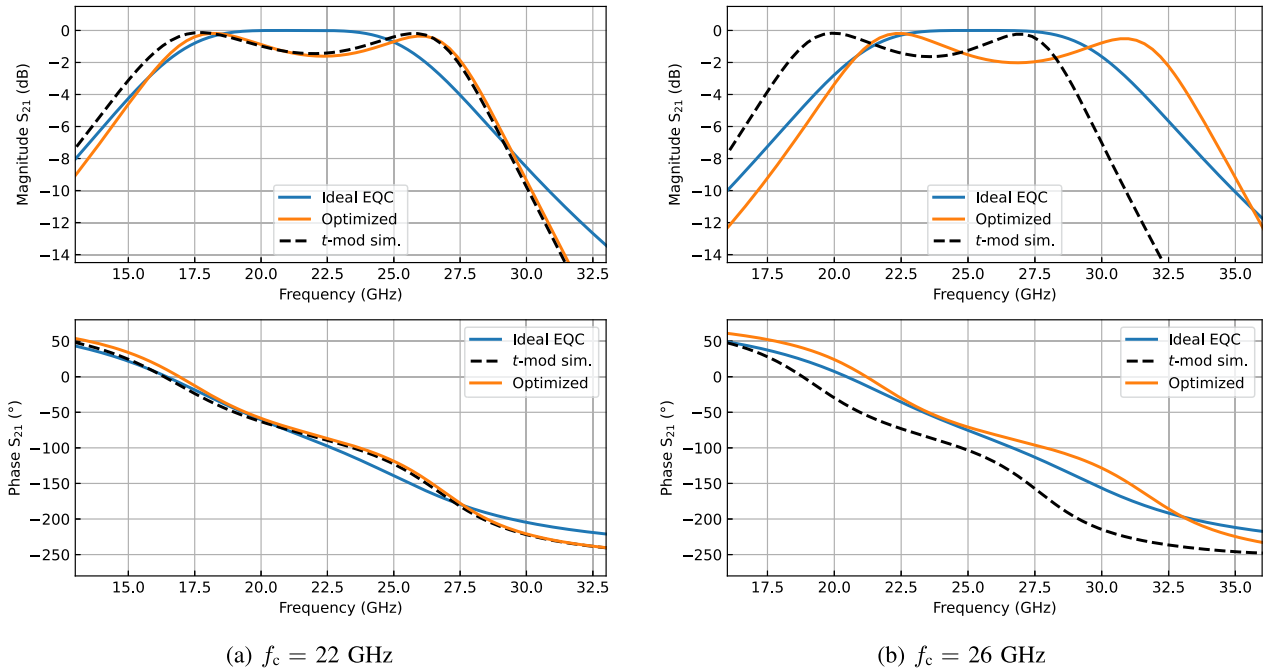
(a) $f_c = 22$ GHz

(b) $f_c = 26$ GHz

FIGURE 4. Frequency responses of analytically extracted and optimized bandpass designs with two different center frequencies. The solid blue curve describes the response of an ideal bandpass corresponding to Fig. 3(b). The dashed curve stands for the simulation results of the analytical design. The finally optimized frequency response, where the simulation matches the ideal bandpass closest, is plotted in orange.

$w_{g,2}$ and $w_{p,2}$ due to the symmetry of the bandpass. Nevertheless, the bandpass designs were optimized using four independent parameters since the fit may require asymmetries over the broad frequency band. The structure periodicity was thereby set to $D = 4$ mm.

Optimization examples for two different bandpass designs with center frequencies at 22 GHz and 26 GHz are presented in Fig. 4. The difference between the ideal bandpass and the simulated structure with analytically extracted parameters for $t = 1.5$ mm are shown together with the optimized frequency response. One can see that the simulation matches the frequency response of the ideal bandpass well in the Fig. 4(a), resulting in an almost consistent curve for the optimization. However, in Fig. 4(b) the simulated response of the analytical design differs from the ideal bandpass. Here, the optimization shifts the final design back to higher frequencies such that it looks similar to the result in Fig. 4(a). It needs to be mentioned that the extracted thickness from (8) matches the actual PCB stack best for the 30 GHz design, but increases with lower center frequencies. Therefore, the deviation between ideal bandpass and simulated design does not solely originate from the fixed PCB thickness, but more from the poor validity of the short transmission line approximation. The optimized structures can finally be utilized as phase shifters. Resulting design parameters of the analytical and optimized solution for the two presented examples are shown in Table 1.

For a better comparison of the analytically generated and simulation optimized resonators, the extracted design parameters are plotted over transmission phase shift at 26 GHz

TABLE 1. Design Parameters of the Ideal Bandpass and Simulation-Based Optimization

Bandpass design	$w_{g,1}$	$w_{p,1}$	$w_{g,2}$	$w_{p,2}$
22 GHz t-mod. EQC	0.397	0.560	0.397	0.560
22 GHz Optimized	0.469	0.589	0.464	0.506
26 GHz t-mod. EQC	0.755	0.430	0.755	0.430
26 GHz Optimized	0.720	0.668	1.071	0.389

All dimensional units are in mm.

in Fig 5. As in [11], linear regression was performed on w_g and w_p from single designs. Examining the resulting regression lines, the calculated grid width from (3) is on average 0.06 mm smaller than the optimization fit, which corresponds to a generally lower layer inductance. Additionally, one can see that the fitted patch gap is rather constant for the optimized designs, whereas the calculated one reduces with increasing phase shift. This implies that the optimization mainly affects the single layer SRS capacitances. Further relating w_p and w_g leads to a reduction of $C_{p,i}$ with increasing SRS grid width. A potential empirical modification of (4) would read then

$$w_p^{emp.}(C_p) = \frac{2(D - w_g)}{\pi} \arcsin\left[\exp\left(-\frac{C_p}{\varepsilon_0 \varepsilon_{eff}} \frac{\pi}{D}\right)\right], \quad (10)$$

where $D - w_g$ in the denominator of the exponential function is replaced by the original periodicity D. Corresponding results for the empirical SRS gap widths are again presented in Fig. 5. Obviously, this adjustment is strongly bound to
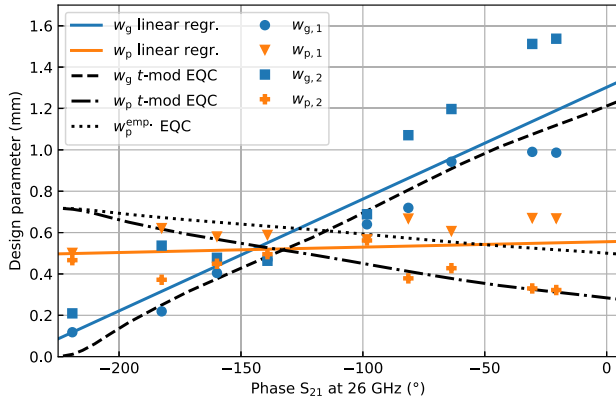
FIGURE 5. Design parameters obtained from the bandpass optimization are plot over transmission phase shift, as in [10]. Linear regression over all w_g and w_p results in a general relation between these parameters and the phase shift. The black dashed, dot-dashed, and dotted lines correspond to the EQC parameters extracted from analytic bandpass solutions.
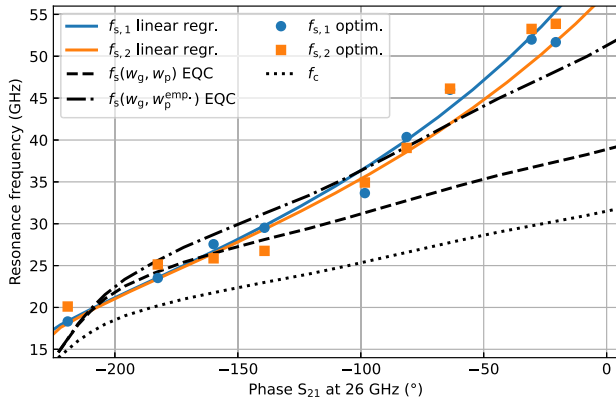

FIGURE 6. Surface resonance frequency f_s plotted over transmission phase shift for optimized SRS structures and EQC design results. The defined bandpass center frequency f_c is added as dotted line.

the results of the optimization procedure and therefore differs from the ideal bandpass designs. However, resulting structures could be utilized without the need of comparably sophisticated gradient optimization.

To investigate the surface resonances of the analytical designs and optimized structures, the SRS grid parameters from Fig. 5 are transformed to EQC parameters ((1) and (2)) and further converted into their surface resonance frequencies

$$f_{s,i} = \frac{1}{2\pi \sqrt{L_g\left(w_{g,i}\right) C_p\left(w_{g,i}, w_{p,i}\right)}}. \quad (11)$$

Corresponding results are presented in Fig. 6. Here one can see that the deviation between analytical and optimized SRS parameters from Fig. 5 leads to increasing resonance frequencies for the optimized designs compared to the EQC solutions. A better fit can be achieved by calculating f_s from the empirically adjusted gap width. Furthermore, an uncoupled system, where the two SRS surfaces are sufficiently apart and not connected through dielectric material, would exhibit same values for f_c and $f_{s,i}$. However, the inter-layer coupling
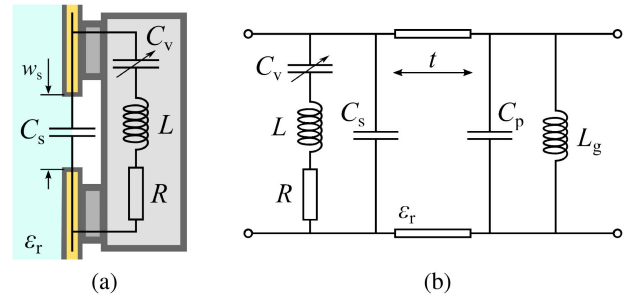

FIGURE 7. Simplified EQCs of (a) varactor soldered to a strip array and (b) the proposed active metasurface with varactors strip array on the left and SRS structures on the right side of a dielectric slab, similarly found in [33].

approximated through L_d and capacitive effect of the dielectric C_d result in higher surface resonance frequencies, even for the EQC solution. In the following, the gained information about SRS surface resonances is used for combinations with active metasurfaces.

IV. SRS COMBINED WITH ACTIVE METASURFACE

The reflectivity of a simple strip array can be tuned by connecting adjacent strips with capacity controllable varactor diodes and biasing them collectively [33]. Since this concept utilizes only a single periodic metal layer, it can be combined with the here investigated SRS structures on a two-layer PCB. The EQC of a corresponding example is shown in Fig. 7. As in [33], the series RLC connection on the left side of the simplified EQC corresponds to the varactor diode with tunable capacitance C_v, component inductance L, and resistance R including mounting parasitics. The periodic strip array beneath the varactors behaves capacitively under TM polarized radiation and is therefore represented by C_s. The shunt capacitance C_p and inductance L_g on the right correspond to the SRS structure at the opposite side of the PCB.

To generate active surfaces that are applicable to lenses and reflectors, the tunable slit array is simulated in combination with different SRS structures. Thereby SRS designs are selected, which exhibit center frequencies within the tuning range of the active grid. In [33], the active metasurfaces were realized with varactor diodes MAVR-000120-1141, bridging a slit gap of $w_s = 0.2$ mm. This resulted in EQC parameters $R = 3.75$ Ω, $L = 0.38$ nH, and C_v between 0.149 pF and 1.0 pF. Investigating solely the active layer with a periodicity of $D = 4$ mm on a $t = 1.5$ mm thick RO4350 PCB gives EQC resonances between 22.5 GHz and 32.2 GHz. The same tuning range is obtained from HFSS simulations with the corresponding RLC boundary parameters $R_{sim} = 4.1$ Ω, $L_{sim} = 0.05$ nH, and C_{sim} from 0.105 pF to 1.25 pF.

V. INVESTIGATION OF FABRICATED SRS STRUCTURES

The optimized, passive SRS metasurfaces as well as the above described combinations with a tunable grid were examined as in [11], [33] on a quasi optical bench [37]. The corresponding measurement setup is depicted in Fig. 8. Like in previous
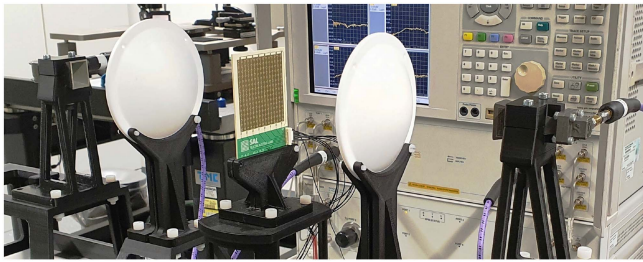
FIGURE 8. Quasi optical bench used to investigate reflection and transmission properties of the designed metasurfaces through OTA S-parameter measurements.
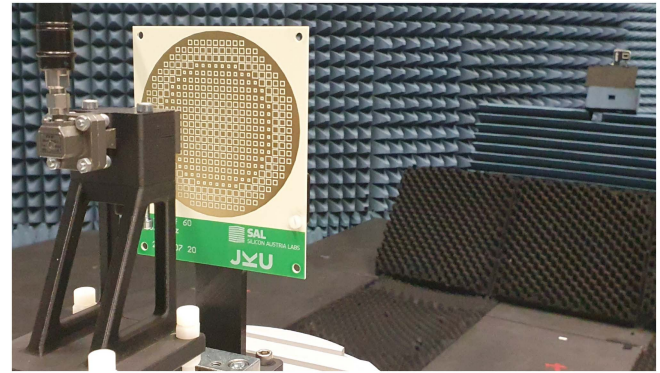

FIGURE 10. Image of lens-antenna beam pattern measurement in anechoic chamber. A horn antenna excites the SRS lens ($f_L = 60$ mm) on a rotary table. The transmitted radiation power is measured over the rotation angle with a second antenna in far-field distance.
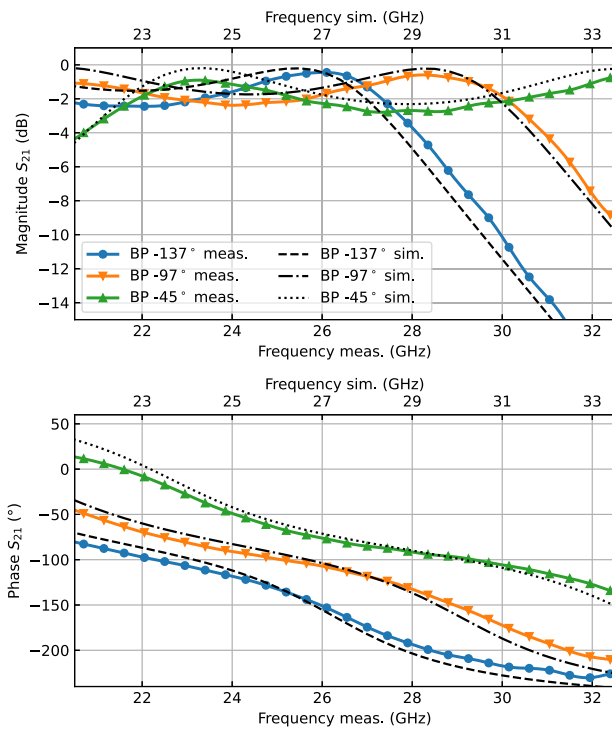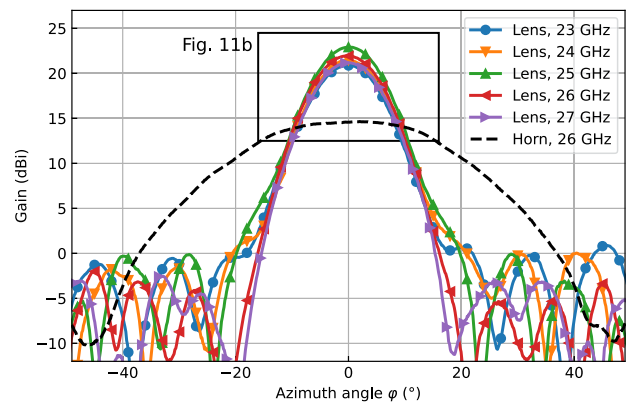

FIGURE 9. Measured and simulated transmission parameters of three SRS bandpass designs that were eventually applied to passive SRS lenses. The simulated S-parameters are shifted by 1 GHz to lower frequencies.

FIGURE 11. Beam patterns of solitary horn and $f_L = 60$ mm lens-antenna measured at different frequencies. (a) Wide angle plot with side-lobes visible. (b) Detailed plot around maximum.
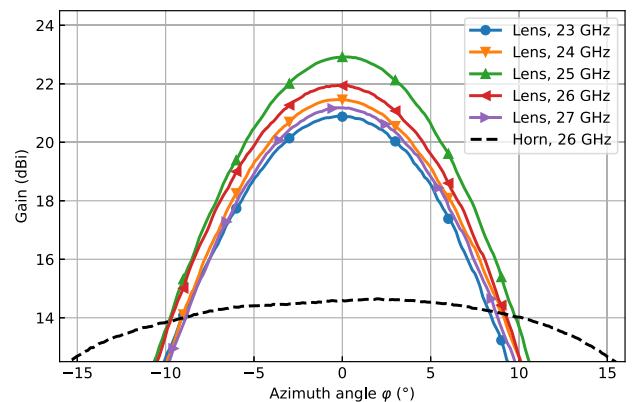
works, the presented frequency responses are time-gated to suppress ripples from reflections between antennas and lenses in the build-up.

In the presented S-parameters plots in Figs. 9 and 13, all simulated frequency responses are shifted down by 1 GHz to better depict the strong correlation between measurements and corresponding HFSS results. This generally present offset could originate from a remaining mismatch between the effective permittivity ε_r used for simulations and design and the actual anisotropic value of the PCB.

For the passive two-layer SRS lenses, several bandpass designs with interpolated parameters were simulated and utilized depending on their transmission magnitude and phase shift. The good conformity of the three frequency responses in Fig. 9 indicates that the created lenses function as expected.

However, their maximum gain is shifted with the simulated S-parameters 1 GHz below their actual design frequency. The same applies to the investigated active structures in Fig. 13, where the coloured, solid lines represent measurements and the unfilled markers depict corresponding HFSS results. Here,
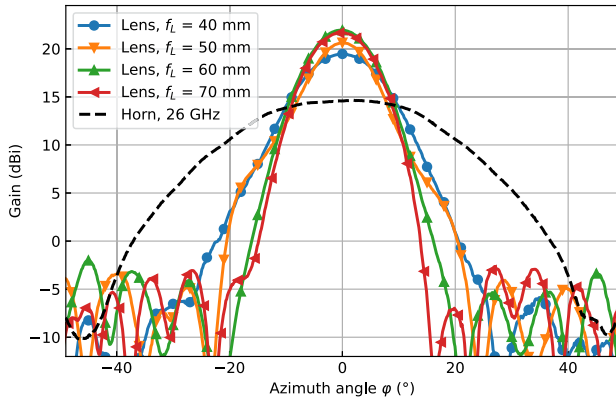
FIGURE 12. Beam patterns of solitary horn and lens-antenna with different focal lengths in millimeter.

the good agreement between measurement and shifted simulation is a strong argument for the simple model in Fig. 7 and [33].

The additional resonance order from the SRS layer on the back side of the active PCB improves its capability as tunable reflector. Compared to the design in [33], the presented structures exhibit a broader tuning bandwidth on the one hand and an increased switching dynamic range on the other hand. Used SRS designs with interpolated phase shifts of $-70°$ and $-45°$ correspond to the center frequencies $f_c^{-70°} \approx 27$ GHz and $f_c^{-45°} \approx 29$ GHz. Additionally, one can assume from [33] that the resonances of the single active surface at 5 V and 8 V are $f_a^{5V} \approx 23.5$ GHz and $f_a^{8V} \approx 25$ GHz, respectively. The resulting notches at 5 V in Fig. 13(a) and 8 V in Fig. 13(b) lie between those two frequencies around their geometrical mean. At these frequencies, both reflectors exhibit a switching dynamic range of around 15 dB with a bandwidth of approximately 1 GHz.

Besides the application as reflectors, the active metasurfaces can also be used for transmission purposes. The plots in Fig. 13(c) and 13(d) exhibit transmission magnitudes above -5 dB for a broad frequency range, enabling the utilization as tunable OTA filters. Furthermore, the surfaces are capable of switching between different transmission phase states, even if the low bandpass order does not allow phase variation over the whole $360°$. However, the combination of several active designs on a single PCB can be used to build active lenses.

VI. PASSIVE LENSES

To build the metasurface lenses, interpolated SRS structures exhibiting different transmission phase shifts $\arg(S_{21})$ are placed on radial positions r at the PCB such that incident, parallel wavefronts interfere constructively at the defined focal plane after transmission. As in [10], [11], [38], the SRS designs have to correct for the phase difference

$$\Delta\varphi = \frac{\sqrt{r^2 + f_L^2} - f_L}{\lambda_0} \cdot 360° \tag{12}$$

that originates from a variation of quasi-optical path lengths, where λ_0 is the wavelength at the design frequency at 26 GHz and f_L is the distance between the metasurface and focal plane, as shown in Fig. 3 in [38].

An SRS lens with a focal length of $f_L = 60$ mm is shown in Fig. 10, where the performance of the lens-antenna is compared to the solitary antenna by measuring the beam pattern of both systems. Thereby, the receive antenna, approximately 3.2 m away from the rotary table, as well as the transmit antenna behind the lens exhibit a maximum gain of 14.6 dBi at 26 GHz. For the antenna-lens combination, the distance between the horn's aperture and the metasurface d was chosen to be 11 mm shorter than the focal length i.e. $d = f_L - 11$ mm, to correct for the phase center position inside the horn antenna. All fabricated passive metasurface lenses exhibit a diameter of $d_L = 95$ mm.

In Fig. 11, the gain of the $f_L = 60$ mm SRS lens is investigated at different frequencies. One can see that the highest maximum gain of $G_{60\,mm} = 22.9$ dBi with a 3 dB-beam width of $11.3°$ for the main lobe occurs at 25 GHz, which is 1 GHz lower than the actual design frequency. This is due to the above mentioned shift between measured and simulated frequency responses, as the transmission magnitude of all bandpass structures is corrupted by simulation model mismatches. However, examining the main lobe shape and first side lobe levels of the different measurements, the 26 GHz beam pattern looks superior. Firstly, the side lobe level ratio at 26 GHz is -26 dB, whereas it only comes to -23 dB at 25 GHz. Secondly, the main lobe at 26 GHz lies closer to the beam pattern of an ideal source, indicating better wavefront shaping by the different bandpass designs.

Besides the investigated metamaterial lens above, other designs exhibiting focal lengths of $f_L = 40, 50,$ and 70 mm were fabricated and verified. The corresponding beam patterns are shown in Fig. 12, where the main lobes become broader with decreasing maximum gain for shorter focal lengths. This indicates that the comparably high gain of the horn antenna leads to selective excitation of the SRS bandpasses. At shorter focal lengths, the feed antenna was placed closer behind the metasurface lens, which resulted in a smaller illumination area for constant feed gain. Hence, the effective radiating area of the lens becomes smaller and its far-field characteristics suffer. Otherwise, this means that more compact systems with smaller lenses can be built at cost of the maximum gain. Depending on the maximum gain resulting from different lenses, their effective aperture area A_e and aperture efficiency e_a can be calculated through

$$A_e = \frac{G_{f_L} \lambda^2}{4\pi} \tag{13}$$

and

$$e_{a,f_L} = A_e \frac{4}{d_L^2 \pi} = G_{f_L} \left(\frac{\lambda}{d_L \pi}\right)^2. \tag{14}$$

For the lens antennas in Fig. 12, the aperture efficiencies read $e_{a,\,40\,mm} = 13.3\%$, $e_{a,\,50\,mm} = 17.1\%$, $e_{a,\,60\,mm} = 23.4\%$, and $e_{a,\,70\,mm} = 22\%$.
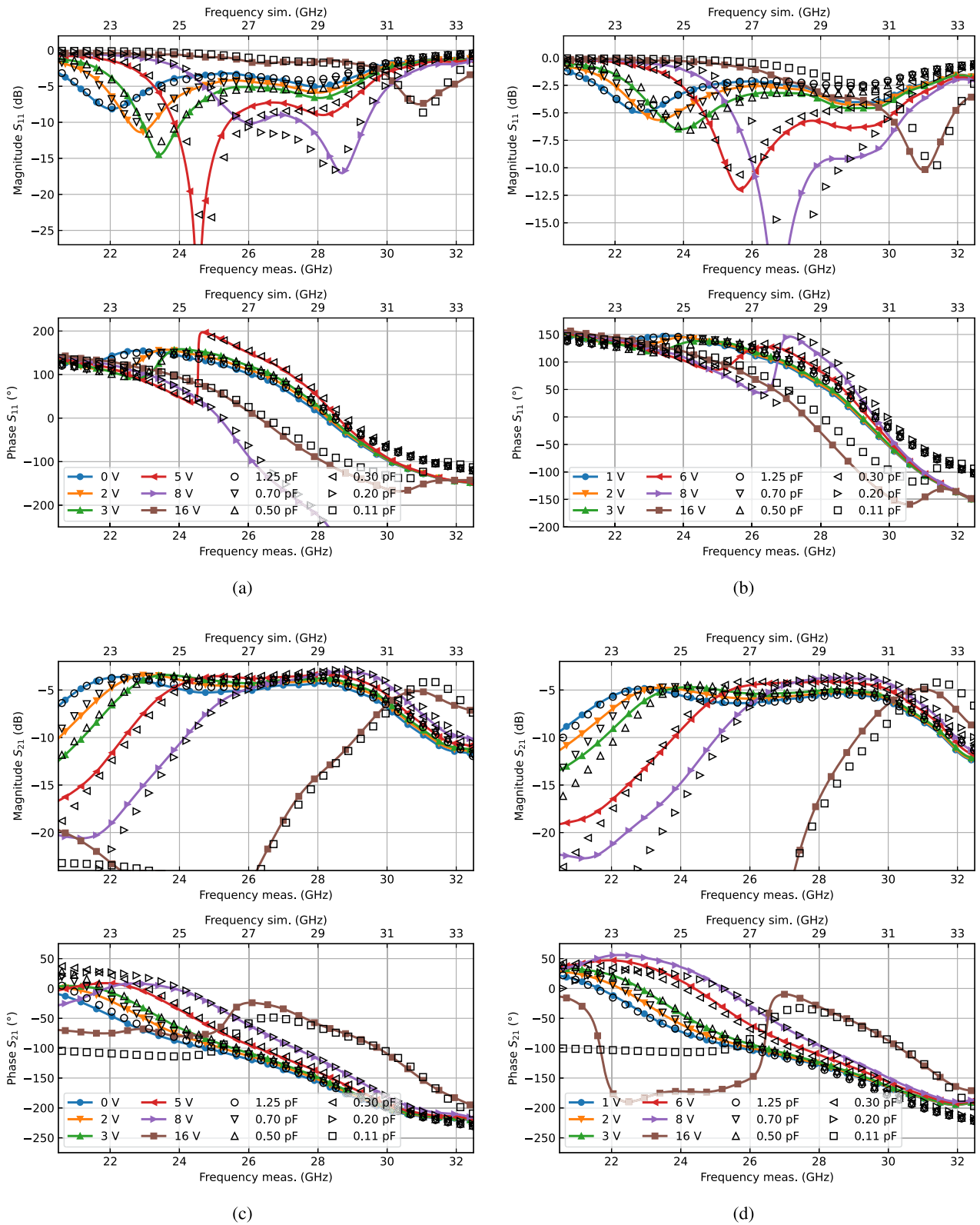
FIGURE 13. Comparison of OTA S-parameter measurements (lines with solid markers) with HFSS simulations (open markers) on two active SRS metasurface designs. The simulated S-parameters are shifted by 1 GHz to lower frequencies. Reflection parameters of combination with −70°-design (a) and −45°-design (b). Transmission parameters for combination with −70°-design (c) and −45°-design (d).

TABLE 2. SRS Lens Performance Compared to Other Thin Metasurface Lens Solutions

ref.	freq. (GHz)	layers	f_L	d_L	G (dBi)	e_a (%)
[8] sim.	39–41	7	50	140	31.7	42.9
[9] sim.	10–10.5	5	100	200	23	43.2
[10]	23.5–24.5	5	50	100	21	19.9
[11]	74–76	5	45	100	31.7	23.9
SRS lens	24–26	2	60	95	21.5	22.8

Dimensional parameters in mm.

A comparison to other passive metamaterial lenses from bandpass unit cells is presented in Table 2. In [8] and [9], the radiation patterns of beams along the optical axis are merely simulation results, which might be a reason for their outstanding aperture efficiency. Nevertheless, reference [9] presents measurements for a lens featuring a 30°-tilted beam, where the maximum gain is about 2.5 dB lower than at the simulations. With this, the corresponding aperture efficiency comes down to 24.3%. Besides, the measured gain and aperture efficiency of the SRS lens antenna is comparable to the author's previous metamaterial lenses, although the used bandpass structures are only of second order.

To optimize the lens system's performance, incident angle dependent transmission phase shifts have to be taken into account in the PCB design process. Additionally, the chosen excitation antenna needs to illuminate the whole effective lens area but should not radiate further sideways. Side lobes can be suppressed by tapering the transmission magnitudes of bandpass designs at the lens border.

VII. ACTIVE LENS

Additionally to the passive lenses above, different active SRS combinations, presented in Section IV, were used to create an active, phase shaping design that operates at 26 GHz. Thereby, the 60×60 mm^2 active lens focused merely along a single dimension, as the slit array combinations allow tuning voltage variations only within one direction. Perpendicular to the tunable slits, SRS designs were placed symmetrically around the center line, variing with the radius. This helped maintaining sufficient transmission phase shift across the lens, as the phase variation from electrical tuning is limited within the transmission band (see Fig. 13).

Similar to the beam pattern measurements on passive lenses, a rotary table that was located 3.5 m apart from a receiving horn antenna was used. With the active metasurface, however, the antennas were rotated by 90°, as the slits have to be excited under TM polarization. Furthermore, the different slits were biased through clamps that were mounted on the rotary table. Images of the build-up with metasurface are shown in Fig. 14(a) and 14(b).

With the given restrictions above, the active metasurface lens should be able to tune its observed focal length and switch to reflection mode, where transmission is blocked completely.
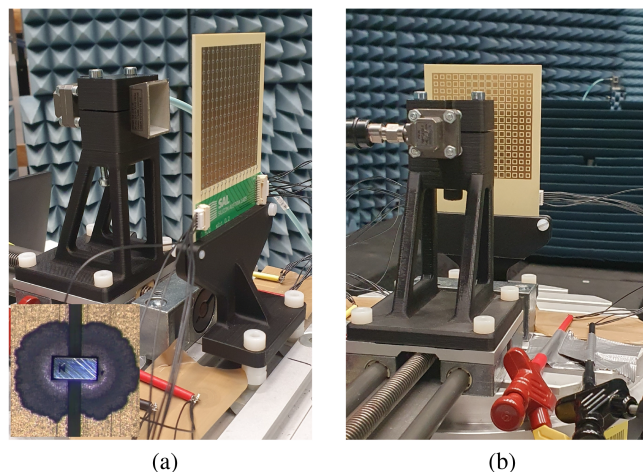
FIGURE 14. Images of active lens-antenna measurements from the front-left (a) and from the back (b). The varactors at the front are biased through connections to the grid. The back side shows a variation of SRS structures from the center to the edge of the sample.

This is achieved by calculating the required transmission phase shifts at the different unit cell positions for the focal lengths 45 mm ("focus I") and 60 mm ("focus II") and selecting corresponding designs that can represent both phase states. These states are presented in Table 3, together with the corresponding SRS design. The necessary varactor bias voltages between two sides of each slit for the three lens states are shown in Table 4. It is mentionable, that the 75° transmission phase shift of the outer elements in "focus I" cannot be achieved by the two layer system and was therefore set to "reflect".

Resulting beam patterns of the active antenna-lens combination are shown in Fig. 15, where three bias states at different focus distances d are compared to the pattern of the reference horn antenna. One can see that the maximum gain of all the beams are close to or below the 14.6 dBi of the horn, which is around 7 dB lower than for the passive lenses. However, this is firstly explained by the one-dimensional focussing of the lens, which approximately halves the additional lens gain (-3.7 dB for the "focus II" state), and secondly by the transmission losses of the metasurface (3 to 4 dB). Due to the already focused excitation of the horn antenna, the smaller size of the active lens compared to the passive one does not matter significantly. The active lens's aperture efficiency is calculated with an aperture area of 60×24.1 mm^2 and results in $e_{a,\,focus\,I} = 16.4\%$ for bias state "focus I" with $d = 34$ mm and $e_{a,\,focus\,II} = 23.1\%$ for bias state "focus II" with $d = 49$ mm. Here, the 60 mm are related to the lens's side length and the 24.1 mm correspond to the long side of the horn feed.

As expected from Fig. 13, nearly all the radiation is blocked in the "reflect" state with all varactors being biased with 16 V. In the "focus I" state, where the focal length should exhibit $f_L = 45$ mm, the maximum gain is larger for shorter distances between antenna aperture and lens. At the same time, the

TABLE 3. Required Transmission Phase Shift and Used SRS Designs for the 15 Varactor Columns

Varactor column #	1	2	3	4	5	6	7	8	9	10	11	12	13	14	15
$\Delta\varphi$ "focus I" (°)	75	0	-45	-90	-135	-150	-180	-180	-180	-150	-135	-90	-45	0	75
$\Delta\varphi$ "focus II" (°)	15	-30	-75	-120	-135	-165	-180	-180	-180	-165	-135	-120	-75	-30	15
SRS designs (°)	10	-16	-45	-97	-137	-165	-191	-191	-191	-165	-137	-97	-45	-16	10

TABLE 4. Varactor Bias and Grid Element Voltages

Varactor column #	1	2	3	4	5	6	7	8	9	10	11	12	13	14	15	
Varator bias "reflect"	16	-16	16	-16	16	-16	16	-16	16	-16	16	-16	16	-16	16	
Varator bias "focus I"	16	-7	7	-8	5	-2	0	-0	0	-2	5	-8	7	-7	16	
Varator bias "focus II"	7	-5	5	-5	2	-0	0	-0	0	-0	2	-5	5	-5	7	
Grid element #	1	2	3	4	5	6	7	8	9	10	11	12	13	14	15	16
Voltage "reflect"	-16	0	-16	0	-16	0	-16	0	-16	0	-16	0	-16	0	-16	0
Voltage "focus I"	-11	5	-2	5	-3	2	0	0	0	0	-2	3	-5	2	-5	11
Voltage "focus II"	-4	3	-2	3	-2	0	0	0	0	0	0	2	-3	2	-3	4

All units are in Volt.

(a)   (b)
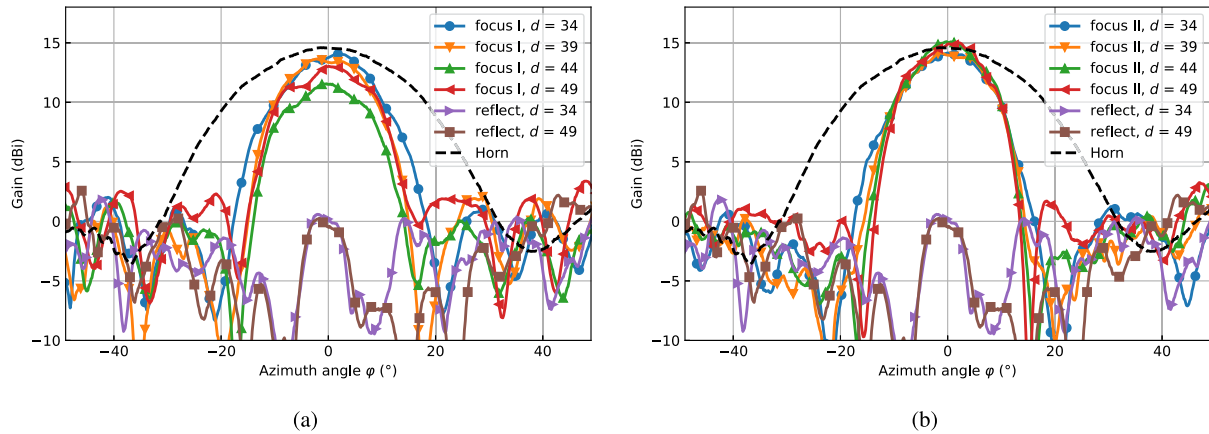
FIGURE 15. Beam patterns of solitary horn and active lens-antenna measured at 26 GHz. Variations of distance between horn aperture and lens *d* in mm with varactor bias "focus I" (a) and "focus II" (b).

maximum gain lies higher for longer distances at the "focus II" state ($f_L = 60$ mm). This coincidence well with prior expectations. Besides the switching between focusing states, the active lens is capable of transmission tuning with at least 12 dB dynamic.

VIII. CONCLUSION
This paper presents the comprehensive investigation of two-dimensional split ring slot structures that are utilized as phase shifting bandpass elements. Thereby, existing approaches are used to model their equivalent circuit parameters, which are further needed to deterministically simulate 2nd-order scatterers on a two-layer PCB. Optimized design parameters are put into relation with transmission phase shifts and oscillation frequencies. In the end, this information is used to generate

active and passive phase manipulating devices that were fabricated and verified.

Considering the fact that all metasurfaces are based on simple two-layer structures, passive lenses exhibit close to ideal beam patterns with high maximum gain at simultaneously low side lobes. Additionally, the tuning bandwidth and switching dynamic range of presented active reflectors are significantly higher compared to other solutions operating at similar frequencies. The active lens design shows clear distinctions between the beam patterns of the different switching states. These findings may be utilized in future radar systems, where an adjustable field-of-view and high gain is of great interest for automated processes in. e.g. automotive or industrial environments.

Nevertheless, to enable full beam steering through active lenses, the tuning range between transmission phase shifts

needs to be increased. This would be possible by combining multiple active layers, which can be additionally supported by split ring slot structures. Generally, a higher number of metal sheets at the metasurface would increase the number of surface resonators and consequently the performance of lenses and reflectors.

ACKNOWLEDGMENT

REFERENCES

[1] S. B. Glybovski, S. A. Tretyakov, P. A. Belov, Y. S. Kivshar, and C. R. Simovski, "Metasurfaces: From microwaves to visible," *Phys. Rep.*, vol. 634, pp. 1–72, May 2016, doi: 10.1016/j.physrep.2016.04.004.

[2] A. Li, S. Singh, and D. Sievenpiper, "Metasurfaces and their applications," *Nanophotonics*, vol. 7, no. 6, pp. 989–1011, Jun. 2018, doi: 10.1515/nanoph-2017-0120.

[3] B. A. F. Esmail, S. Koziel, and S. Szczepanski, "Overview of planar antenna loading metamaterials for gain performance enhancement: The two decades of progress," *IEEE Access*, vol. 10, pp. 27381–27403, 2022, doi: 10.1109/access.2022.3157634.

[4] K. Iqbal and Q. U. Khan, "Review of metasurfaces through unit cell design and numerical extraction of parameters and their applications in antennas," *IEEE Access*, vol. 10, pp. 112368–112391, 2022, doi: 10.1109/access.2022.3214319.

[5] C. Liaskos et al., "A new wireless communication paradigm through software-controlled metasurfaces," *IEEE Commun. Mag.*, vol. 56, no. 9, pp. 162–169, Sep. 2018, doi: 10.1109/mcom.2018.1700659.

[6] S. Tiwari, A. K. Singh, A. K. Poddar, U. L. Rohde, and A. Dubey, "Active beamsteerable digital metasurface lens antenna for millimeter-wave applications," *IEEE Antennas Wireless Propag. Lett.*, vol. 22, no. 12, pp. 2871–2875, Dec. 2023, doi: 10.1109/lawp.2023.3303135.

[7] M. A. Al-Joumayly and N. Behdad, "Wideband planar microwave lenses using sub-wavelength spatial phase shifters," *IEEE Trans. Antennas Propag.*, vol. 59, no. 12, pp. 4542–4552, Dec. 2011, doi: 10.1109/tap.2011.2165515.

[8] S. Foo, "Millimeter-wave TTD metamaterial fresnel lens," in *Proc. IEEE Int. Symp. Antennas Propag. USNC/URSI Nat. Radio Sci. Meeting*, 2017, pp. 2649–2650, doi: 10.1109/apusncursinrsm.2017.8073367.

[9] J. Han, L. Li, T. Zhang, and R. Xi, "Control and improvement of antenna gain by using multilayer non-uniform metasurfaces," *EPJ Appl. Metamaterials*, vol. 6, 2019, Art. no. 4, doi: 10.1051/epjam/2019003.

[10] C. Kohlberger, G. Hueber, C. Wagner, and A. Stelzer, "Gradient optimization on third order bandpasses for a 24 GHz metasurface lens," in *Proc. 50th Eur. Microw. Conf.*, 2021, pp. 579–582, doi: 10.23919/eumc48046.2021.9338163.

[11] C. Kohlberger, R. Huttner, and A. Stelzer, "Metamaterial lens for monopulse beamforming with a 77-GHz long-range radar," in *Proc. IEEE 51st Eur. Microw. Conf.*, 2022, pp. 253–256, doi: 10.23919/eumc50147.2022.9784199.

[12] O. Luukkonen et al., "Simple and accurate analytical model of planar grids and high-impedance surfaces comprising metal strips or patches," *IEEE Trans. Antennas Propag.*, vol. 56, no. 6, pp. 1624–1632, Jun. 2008, doi: 10.1109/tap.2008.923327.

[13] S. Zhang et al., "3D-printed planar graded index lenses," *IET Microw., Antennas Propag.*, vol. 10, no. 13, pp. 1411–1419, 2016, doi: 10.1049/iet-map.2016.0013.

[14] R. K. Arya, S. Pandey, and R. Mittra, "Flat lens design using artificially engineered materials," *Prog. Electromagn. Res. C*, vol. 64, pp. 71–78, 2016, doi: 10.2528/pierc16021302.

[15] R. K. Arya et al., "Meta-atoms and artificially engineered materials for antenna applications," in *Developments in Antenna Analysis and Design: Volume 1*. Electromagn. Acad.: IET, 2008, pp. 351–405, doi: 10.1049/sbew543f_ch10.

[16] B. Zhu, Y. Feng, J. Zhao, C. Huang, and T. Jiang, "Switchable metamaterial reflector/absorber for different polarized electromagnetic waves," *Appl. Phys. Lett.*, vol. 97, no. 5, 2010, Art. no.051906, doi: 10.1063/1.3477960.

[17] X. Zeng, M. Gao, L. Zhang, G. Wan, and B. Hu, "Design of a tuneable and broadband absorber using a switchable transmissive/reflective FSS," *IET Microw., Antennas Propag.*, vol. 12, no. 7, pp. 1211–1215, 2018, doi: 10.1049/iet-map.2017.0691.

[18] D. Sievenpiper, J. Schaffner, H. Song, R. Loo, and G. Tangonan, "Two-dimensional beam steering using an electrically tunable impedance surface," *IEEE Trans. Antennas Propag.*, vol. 51, no. 10, pp. 2713–2722, Oct. 2003, doi: 10.1109/tap.2003.817558.

[19] B. Ratni, A. de Lustrac, G.-P. Piau, and S. N. Burokur, "Active metasurface for reconfigurable reflectors," *Appl. Phys. A*, vol. 124, no. 2, pp. 1–8, Jan. 2018, doi: 10.1007/s00339-017-1502-4.

[20] R. Langley and E. Parker, "Equivalent circuit model for arrays of square loops," *Electron. Lett.*, vol. 18, no. 7, pp. 294–296, 1982, doi: 10.1049/el:19820201.

[21] C. Lee and R. Langley, "Equivalent-circuit models for frequency-selective surfaces at oblique angles of incidence," *IEE Proc.-Microw., Antennas Propag.*, vol. 132, no. 6, pp. 395–399, 1985, doi: 10.1049/ip-h-2.1985.0070.

[22] A. E. Yilmaz and M. Kuzuoğlu, "Design of the square loop frequency selective surfaces with particle swarm optimization via the equivalent circuit model," *Radioengineering*, vol. 18, no. 2, pp. 95–102, 2009. [Online]. Available: https://hdl.handle.net/11511/52651

[23] D. Ferreira, R. F. S. Caldeirinha, I. Cuinas, and T. R. Fernandes, "Square loop and slot frequency selective surfaces study for equivalent circuit model optimization," *IEEE Trans. Antennas Propag.*, vol. 63, no. 9, pp. 3947–3955, Sep. 2015, doi: 10.1109/tap.2015.2444420.

[24] F. Costa and A. Monorchio, "Closed-form analysis of reflection losses in microstrip reflectarray antennas," *IEEE Trans. Antennas Propag.*, vol. 60, no. 10, pp. 4650–4660, Oct. 2012, doi: 10.1109/tap.2012.2207318.

[25] F. Costa, A. Monorchio, and G. Manara, "An overview of equivalent circuit modeling techniques of frequency selective surfaces and metasurfaces," *Appl. Comput. Electromagn. Soc. J.*, vol. 29, no. 12, pp. 960–976, 2014.

[26] X.-D. Hu, X.-L. Zhou, L.-S. Wu, L. Zhou, and W.-Y. Yin, "A miniaturized dual-band frequency selective surface (FSS) with closed loop and its complementary pattern," *IEEE Antennas Wireless Propag. Lett.*, vol. 8, pp. 1374–1377, 2009, doi: 10.1109/lawp.2009.2039110.

[27] T. Hong, W. Xing, Q. Zhao, Y. Gu, and S. Gong, "Single-layer frequency selective surface with angular stability property," *IEEE Antennas Wireless Propag. Lett.*, vol. 17, no. 4, pp. 547–550, Apr. 2018, doi: 10.1109/lawp.2018.2801864.

[28] K. Sarabandi and N. Behdad, "A frequency selective surface with miniaturized elements," *IEEE Trans. Antennas Propag.*, vol. 55, no. 5, pp. 1239–1245, May 2007, doi: 10.1109/tap.2007.895567.

[29] M. Al-Joumayly and N. Behdad, "A new technique for design of low-profile, second-order, bandpass frequency selective surfaces," *IEEE Trans. Antennas Propag.*, vol. 57, no. 2, pp. 452–459, Feb. 2009, doi: 10.1109/tap.2008.2011382.

[30] M. A. Al-Joumayly and N. Behdad, "A generalized method for synthesizing low-profile, band-pass frequency selective surfaces with non-resonant constituting elements," *IEEE Trans. Antennas Propag.*, vol. 58, no. 12, pp. 4033–4041, Dec. 2010, doi: 10.1109/tap.2010.2078474.

[31] D. Wang, Y. Chang, W. Che, and Y. L. Chow, "Miniaturized dual-band loaded frequency selective surface with narrow band spacing," in *Proc. IEEE Int. Conf. Microw. Millimeter Wave Technol.*, 2012, pp. 1–4, doi: 10.1109/icmmt.2012.6230420.

[32] C. Kohlberger and A. Stelzer, "Multi-modal scattering and propagation through several close periodic grids," *IEEE Trans. Antennas Propag.*, vol. 70, no. 7, pp. 5758–5769, Jul. 2022, DOI: 10.1109/tap.2022.3161327.

[33] C. Kohlberger, A. Kearns, and A. Stelzer, "A tunable K-band reflector," *IEEE Antennas Wireless Propag. Lett.*, vol. 22, no. 2, pp. 328–332, Feb. 2023, doi: 10.1109/lawp.2022.3210225.

[34] F. Bayatpur and K. Sarabandi, "A tunable metamaterial frequency-selective surface with variable modes of operation," *IEEE Trans. Microw. Theory Techn.*, vol. 57, no. 6, pp. 1433–1438, Jun. 2009, DOI: 10.1109/tmtt.2009.2020841.

[35] K. Zhang, W. Jiang, and S. Gong, "Design bandpass frequency selective surface absorber using LC-resonators," *IEEE Antennas Wireless Propag. Lett.*, vol. 16, pp. 2586–2589, 2017, doi: 10.1109/lawp.2017.2734918.

[36] A. F. Horn, P. A. LaFrance, J. W. Reynolds, and J. Coonrod, "The influence of test method, conductor profile and substrate anisotropy on the permittivity values required for accurate modeling of high frequency planar circuits," *Circuit World*, vol. 38, no. 4, pp. 219–231, 2012, doi: 10.1108/03056121211280431.

[37] J. W. Schultz, *Focused Beam Methods: Measuring Microwave Materials in Free Space*. Scotts Valley, CA, USA: CreateSpace Independent Publishing Platform, 2012.

[38] C. Kohlberger, R. Hüttner, C. Wagner, and A. Stelzer, "Metamaterial lenses for monostatic and bistatic 77 GHz radar systems," *Int. J. Microw. Wireless Technol.*, vol. 15, no. 6, pp. 1021–1026, 2003, doi: 10.1017/s1759078722001337.

CHRISTOPH KOHLBERGER (Graduate Student Member, IEEE) was born in Freistadt, Austria, in 1991. He received the Dipl.Ing. degree in technical physics from Johannes Kepler University Linz, Linz, Austria, in 2018. He is currently working toward the Ph.D. degree in electronics and information technology with the Institute for Communications Engineering and RF Systems. In 2018, he joined Silicon Austria Labs GmbH, where he worked on an industry cooperative project as a Scientist with Millimeter Wave Technologies Group. He is currently radar algorithm Engineer with the Flight Physics Group, Joby Austria GmbH, Linz. His research interests include optics, electromagnetics, RF metasurfaces, their modeling, and related applications and novel concepts for radar imaging systems.

SAEID KARAMZADEH (Member, IEEE) received the M.S. and Ph.D. degrees from the Department of Communication Systems, Satellite Communication and Remote Sensing Program, Istanbul Technical University, Istanbul, Türkiye, in 2013 and 2015, respectively. He is currently a Senior Scientist with the Millimeter Wave Technologies Unit, Intelligent Wireless Systems Division of Silicon Austria Labs, and also holds a full professorship with the Electrical and Electronics Engineering Department, Faculty of Engineering and Natural Sciences, Bahçeşehir University, Istanbul. His research interests include remote sensing, radar, microwave, and antenna design. He was the recipient of the most successful Ph.D. Thesis Award from Istanbul Technical University.

ANDREAS STELZER (Member, IEEE) received the diploma engineer degree in electrical engineering from the Technical University of Vienna, Vienna, Austria, in 1994, and the Ph.D. degree (Dr. techn.) in mechatronics (with honors sub auspiciis praesidentis rei publicae) from Johannes Kepler University Linz, Linz, Austria, in 2000.

In 2003, he was an Associate Professor with the Institute for Communications Engineering and RF Systems, Johannes Kepler University Linz. Since 2008, he has been a key Researcher for the Austrian Center of Competence in Mechatronics, where he is responsible for numerous industrial projects. In 2007, he was granted a Christian Doppler Research Laboratory for Integrated Radar Sensors. Since 2011, he has been a full Professor with the Johannes Kepler University Linz, heading the Department for RF-Systems. He is a co-founder of company Inras, where industrial radar sensors are developed. Since 2020, he has been the Head of the joint Linz Institute of Technology and Silicon-Austrian-Labs Millimeter-Wave Lab working on combined sensing and communication applications for future 6G.

He has authored or coauthored more than 430 journal, conference, and workshop contributions. His research interests include microwave sensor systems for industrial and automotive applications, integrated radar sensor concepts, SiGe based circuit design, microwave packaging in eWLB, RF and microwave subsystems, surface acoustic wave sensor systems and applications, and digital signal processing for sensor signal evaluation. He was an Associate Editor for IEEE MICROWAVE AND WIRELESS COMPONENTS LETTERS. He was the Chair of MTT-27 Wireless-Enabled Automotive and Vehicular Applications. He was the recipient of several awards including the 2008 IEEE Microwave Theory and Techniques Society Outstanding Young Engineer Award, 2011 IEEE Microwave Prize, and Best Paper Award of the International Journal of Microwave and Wireless Technologies 2016. He was the co-recipient of the 2012 European Conference on Antennas and Propagation Best Measurement Paper Prize, 2012 Asia Pacific Conference on Antennas and Propagation Best Paper Award, 2011 German Microwave Conference Best Paper Award, and EEEfCOM Innovation Award, and European Microwave Association (EuMA) Radar Prize of the European Radar Conference 2003. He is a member of IEEE MTT, IM, and CAS Societies. He is a member of Austrian ÖVE. He was a IEEE Distinguished Microwave Lecturer from 2014 to 2016 and Chair of IEEE International Conference on Microwaves for Intelligent Mobility in 2020.